

Article

Insight into Dynamic of Mono and Hybrid Nanofluids Subject to Binary Chemical Reaction, Activation Energy, and Magnetic Field through the Porous Surfaces

Qadeer Raza ^{1,†}, M. Zubair Akbar Qureshi ¹, Behzad Ali Khan ¹, Ahmed Kadhim Hussein ^{2,3} , Bagh Ali ⁴ , Nehad Ali Shah ^{5,†}  and Jae Dong Chung ^{5,*} 

¹ Department of Mathematics, AIR University, Multan Campus, Multan 49501, Pakistan

² Mechanical Engineering Department, College of Engineering, University of Babylon, Hilla 00964, Iraq

³ College of Engineering, University of Warith Al-Anbiyaa, Karbala 56001, Iraq

⁴ Faculty of Computer Science and Information Technology, Superior University, Lahore 54000, Pakistan

⁵ Department of Mechanical Engineering, Sejong University, Seoul 05006, Korea

* Correspondence: jdchung@sejong.ac.kr

† These authors contributed equally to this work and are co-first authors.

Abstract: The mathematical modeling of the activation energy and binary chemical reaction system with six distinct types of nanoparticles, along with the magnetohydrodynamic effect, is studied in this paper. Different types of hybrid nanofluids flowing over porous surfaces with heat and mass transfer aspects are examined here. The empirical relations for nanoparticle materials associated with thermophysical properties are expressed as partial differential equations, which are then interpreted into ordinary differential expressions using appropriate variables. The initial shooting method converts the boundary condition into the initial condition with an appropriate guess and finally finds out an accurate numerical solution by using the Runge–Kutta method with numerical stability. Variations in nanoparticle volume fraction at the lower and upper walls of porous surfaces, as well as the heat transfer rate measurements, are computed using the controlling physical factors. The effects of the flow-related variables on the axial velocity, radial velocity, temperature, and concentration profile dispersion are also investigated. The Permeable Reynolds number is directly proportional to the regression parameter. The injection/suction phenomenon associated with the expanding/contracting cases, respectively, have been described with engineering parameters. The hybrid nanoparticle volume fraction (1–5%) has a significant effect on the thermal system and radial velocity.

Keywords: hybrid nanofluids; chemical reaction; activation energy; porous surface

MSC: 76D05; 76W05; 76-10



Citation: Raza, Q.; Qureshi, M.Z.A.; Khan, B.A.; Kadhim Hussein, A.; Ali, B.; Shah, N.A.; Chung, J.D. Insight into Dynamic of Mono and Hybrid Nanofluids Subject to Binary Chemical Reaction, Activation Energy, and Magnetic Field through the Porous Surfaces. *Mathematics* **2022**, *10*, 3013. <https://doi.org/10.3390/math10163013>

Academic Editor: Vasily Novozhilov

Received: 14 July 2022

Accepted: 18 August 2022

Published: 21 August 2022

Publisher's Note: MDPI stays neutral with regard to jurisdictional claims in published maps and institutional affiliations.



Copyright: © 2022 by the authors. Licensee MDPI, Basel, Switzerland. This article is an open access article distributed under the terms and conditions of the Creative Commons Attribution (CC BY) license (<https://creativecommons.org/licenses/by/4.0/>).

1. Introduction

To fulfill the requirement for a superior fluid with high thermal conductivity, the term “hybrid nanofluids” refers to a novel class of nanofluids that has been created. Hybrid nanofluids are a type of nanofluid that contain two separate nanoparticles dispersed in the same fluid. Applications for hybrid nanofluids that exceed nanofluids in terms of efficiency include electronic chilling, producing refrigeration, fluid in machining, reactor system temperature management, inversion temperature control, biomedical and pharmaceutical elimination, and cooling systems. To improve it even more, hybrid nanofluids are instigated. Unsettled hydro-magnetic heat transport mixed nanofluids slide past a stretching sheet with heat energy, biochemical mechanisms, vacuum, and slippage effects, according to Sreedevi et al. [1]. Roy et al. [2] investigated the thermal transport of a hybrid nanofluid flow through a porous plate governed by a binary chemical process regulated by chemical potential. Using a generalized hybrid nanofluids model, Xue et al. [3] evaluated

hybrid nanofluids flow with various types of nanoparticles. The flow stability of hybrid nanofluids between two simultaneous and static plates packed with porous media was examined by Pascaline et al. [4]. Maskeen et al. [5] used pure water as the basis fluid to evaluate the increase of heat transfer in MHD alumina-copper hybrid nanofluids flowing over the stretched surface of the cylinder. In the presence of rotation, Devi et al. [6] examined the consequences of hybrid nanofluids on stretching sheets. They also looked at the impact of the Lorentz effect and statistically examined it. Sahoo et al. [7] used a variety of nanoparticles to investigate the various mixes to determine the highest heat transfer rate. Three nanoparticles were considered in this study, and, as well as ternary hybrid nanofluids. Aladdin et al. [8] viewed the presence of suction under a field magnetism environment by using hybrid nanofluids flowing over a moving plate. Waini et al. [9] studied nanofluids of the fusion-type flowing over singularly perturbed stretching surfaces. Hayat et al. [10] investigated hybrid nanofluids and discovered that they have a higher heat transfer capacity than simple nanofluids. The creation of hybrid nanofluids with high durability and enhanced thermal diffusivity, according to Das et al. [11], is significant because it enhances thermal system efficiency, and it could contribute to energy quality and productivity. In the presence of the Lorentz force and thermal radiation over a permeable moving surface, Zainal et al. [12] studied the flow and heat transmission characteristics of hybrid nanofluids. Devi et al. [13] retrieved the activity of hybrid nanofluids by accounting for nanocrystals' substantial density fractions. Chahregh et al. [14] highlighted the use of a porous tube to move biological fluids, such as hybrid nanofluids, via an artery for medicine administration and blood circulation in the respiratory system. When compared to pure race, Dinarvand et al. [15] found that nanocomposites diminish the cardiovascular influence of the capillary. Furthermore, the blood speed decreases as the magnetization increases. According to Shahsavari et al. [16], the latest direction of using hybrid nanofluids as efficient heat transfer fluids in all thermal management applications appears promising. Ahammed et al. [17] analyzed the heat and mass transport capabilities of hybrid nanofluid flow in a mini channel in an experimental environment. Chamkha et al. [18] looked into hybrid nanofluids and discovered that, in a rotating system, "Nusselt number is a function of infusion and emission parameters, as well as the size distribution, in a sorted array of nanofluids". Bhattad et al. [19] evaluated the temperature difference and flow rate properties of MWCNT–water hybrid nanofluids on a heat converter plate and discovered a 39.16 percent increase in the factor of convection. Hussien et al. [20] studied the heat transfer of GNPs/MWCNTs–water-blended features of nanofluids flowing through a miniature and reported a 43.4 percent increase in the heat transfer rate. Soltani and Akbari [21] explored the impact of the temperature and particle concentration on the stiffness progression of MgO–MWCNT/EG hybrid nanofluids. Zahra et al. [22] examined the consolidation power of nonmaterials such as nanoscale metals and nanostructured materials in a novel with a high-energy biocomposite, which should result in exciting qualities that combine the advantages of each nanocomponent. It was determined by Khilap Singh et al. [23] that the impact of chemical reaction on the heat and mass transfer flow of a micropolar fluid in a porous channel with heat production and thermal radiation is being explored. Odelu Ojjela et al. [24] describe an incompressible two-dimensional thermal and mass transfer of an electrically conducting micropolar fluid flow in a porous media among two parallel plates including chemical reaction, Hall, and ion slip effects. According to Nepal Chandra Roy et al. [25], theoretical research has been done on the flow and heat transmission of transient free convection of a hybrid nanofluid between two parallel surfaces. A. M. Jyothi et al. [26] studied the behavior of a Casson hybrid nanofluid squeezing flow across two parallel plates with the influence of a thermal supply and thermophoretic particle accumulation. This paper examines the unsteady magnetohydrodynamic heat and mass transfer analysis of hybrid nanofluid flow across a stretched surface with chemical reaction, suction, slip effects, and thermal radiation by Muttukuru Santhi et al. [27]. Muhammad Bilal et al. [28] investigated the simultaneous impact of magnetic and electrohydrodynamic forces on the flow of water-based iron ox-

ide and carbon nanotubes hybrid nanoliquids among two moving plates. According to G. K. Ramesh [29], the study conveys the flow, thermal, and mass transfer of a hybrid nanofluid across parallel plates by combining chemical processes, activation energy, and heat source/sink effects. M. Shanmugapriya et al. [30] have incorporated the impact of a magnetic field, thermal radiation, and activation energy with a binary chemical reaction to accurately explore the precise point of hybrid nanofluids flow. Many researchers have focused on this concept, and the areas of interest may be found in writing, such as Refs. [31–34].

In 1889, for the first time, the phrase stimulation intensity was coined by a Swedish scientist, Svante Arrhenius. In the heat and mass transmission, stimulation strength and binary chemical reactions exist, with electrochemistry, subsurface aquifers, dispersions of varied solutions, and food manufacturing among the possibilities, as well as other areas. The concept of binary chemical reactions with activation energy was first used by Bestman et al. [35]. Khan et al. [36] looked at how a dual chain reaction affected the flow of a nanofluid across a surface with stimulation strength. Jayadevamurthy et al. [37] analyzed the bioconvective flow of hybrid nanofluids over a motorist disc with activation energy. Reddy et al. [38] investigated the characteristics of activation energy with chemical reactions in the magnetohydrodynamic movement of mixed nanoparticles. Mustafa et al. [39] investigated the activation energy in the mixed convection flow movement of magnetic properties distribution on an elastic region with no flux at the border, where the perfusion of warmth on account of the border was minimized as the chemical reaction rate increased. Bhatti and Michaelides [40] have provided a numerical result on the activation energy of thermo-bio convection nanofluids flowing across a plate.

On the other hand, using hybrid nanofluids on a porous surface to improve aspects of forced convection in industrial operations is a very efficient approach. As a result, researchers have given porous media techniques a lot of thought. Kasaeian et al. [41] studied how nanofluids move through porous media and how they transfer heat. The boundary layer equations were explored by Singh et al. [42], using a porous structure over a superliner stretching plate. Subhani et al. [43] utilized fluid theory to investigate the MHD flow of based nano moisture in a time-dependent manner across a spongy rotating surface. Al-Zamily [44] investigated the heat transport of water nanofluids in a hollow with a porous cliff layer. Fadhilah et al. [45] investigated the transport of heat and the stalling point in unstable nanofluids across a porous surface that is exponentially stretching/shrinking. Numerous practical devices, including hydromagnetic generators, electromagnetic pumps, and flow meters, use magnetohydrodynamic (MHD) fluxes across porous surfaces. The significance of MHD convective flows involving temperature distribution in the construction of MHD producers and accelerators in geophysics, as well as in systems like subsurface water and energy storage, has reignited interest in these phenomena. In addition to viscous dissipation, some energy is also stored in the fluid as strain energy when an elastic–viscous fluid is forced to flow as a result of applied stress. While we are concerned with the rate of strain in a viscous fluid that is inelastic, we cannot ignore any strain, no matter how minute, because it ultimately causes the fluid to return to its original condition. When the tension is eliminated, only elastic–viscous liquid experiences some recovery from the strain, whereas the entire strain is retained in other liquids. To make the mathematical analysis of the MHD convective flow experiments more straightforward, the Hall current and ion slip factors in Ohm’s law were disregarded. However, the importance of the ion slip and the Hall current is crucial for the presence of a high magnetic field. Determining the effect of the Hall current and the ion slip factors in the MHD equations is therefore necessary for several physical conditions. According to Obai Younis et al. [46], the research investigation was the first to examine the numerical methods of the MHD-free convective thermal transport and its connection with radiation over a hot source within a porous semicircular cavity filled with SWCNTs–water nanofluid. The major purpose of this experiment, according to Quanfu Lou et al. [47], was to evaluate the temperature and momentum transfer of rotating dusty micropolar fluid flow with the persistence of transmitting particulate matter

throughout the extending sheet. It was due to Muhammad Zeeshan Ashraf et al. [48] that this numerical solution significantly developed into a novel computational approach for stable magnetohydrodynamic convective flows of tangent hyperbolic nanofluid traversing a nonlinearly elongating elastic surface with a variable thickness. Mehran et al. [49] demonstrated that, when hybrid nanofluids flow through absorbent materials, heat transmission increases due to the magnetic field and convection influences. In the influence of high magnetic and chemical change effects, Mallikarjuna et al. [50] investigated the linked thermal transport by free convection flow of a Newtonian fluid around a revolving conform immersed in microchannels. Numerous researchers have studied the MHD effects in conjunction with varied geometries and outcomes [51–53].

The main goal of this work is to conduct a mathematical investigation of the heat and mass transmission elements of various combinations of nanoparticles subject to flowing across movable plates with activation energy, chemical reaction, and Lorentz force effects. Analysis of the mono and hybrid nanofluids, together with velocity, heat, and mass transfer enhancement effects, flow through up and down moving porous plates. For this purpose, we consider unsteady, laminar, MHD, incompressible, two-dimensional mono and hybrid nanofluids passing through porous surfaces. Motivated by the above-mentioned wide scope of application and the unusual thermal conductivity of the nanosized nanoparticles, we decided to elaborate on the present fluid model. A mathematical model has been developed for the thermophysical properties of hybrid nanofluids for metallic/metallic-oxides nanoparticles. We achieved a nonlinear system of ODEs by applying appropriate similarity transformation on the governing momentum, energy, and concentration equations. The new ODEs mathematical model with hybrid correlations based on the nanoparticles volume fraction, permeable Reynolds number, Prandtl number, expanding/contracting parameter, activation energy, chemical reaction, and different nondimensional parameter has been described through graphs and tables in detail. Using the fourth order Runge–Kutta integration method and the shooting approach, this boundary value issue, the system of ODE’s model, was numerically solved.

2. Mathematical Formulation

Consider a physical scenario in which a 2D, time-dependent, laminar, noncompressible, Newtonian trihybrid nanofluids flow of the transmission of heat and mass among two concentrations moving porous surfaces with permeability in the presence of an external magnetic field Bo is monitored, where the x -axis is horizontal, measured along the surface, and y is vertical to it (See Figure 1). Furthermore, the Cartesian coordinates are x and y , followed by the plates. The generated magnetic field is disregarded based on the premise of a low Reynolds number. Further, the fluid is considered stable and ignored by the agglomeration of tiny particles. Mono and hybrid nanofluids’ thermos physical features are listed in detail in Table 1, and Table 2 shows the values of several base fluids and NPs. The law of conservation of momentum, energy, and concentration is applied to a binary chemical process represented by the activation energy:

$$\frac{\partial u}{\partial x} + \frac{\partial v}{\partial y} = 0 \tag{1}$$

$$\frac{\partial u}{\partial t} + u \frac{\partial u}{\partial x} + v \frac{\partial u}{\partial y} = -\frac{P_x}{\rho_{hnf}} + v_{hnf} \left(\frac{\partial^2 u}{\partial x^2} + \frac{\partial^2 u}{\partial y^2} \right) - \frac{\sigma_e B_0^2}{\rho_{hnf}} u \tag{2}$$

$$\frac{\partial v}{\partial t} + u \frac{\partial v}{\partial x} + v \frac{\partial v}{\partial y} = -\frac{P_y}{\rho_{hnf}} + v_{hnf} \left(\frac{\partial^2 v}{\partial x^2} + \frac{\partial^2 v}{\partial y^2} \right) \tag{3}$$

$$\frac{\partial T}{\partial t} + u \frac{\partial T}{\partial x} + v \frac{\partial T}{\partial y} = \alpha_{hnf} \left(\frac{\partial^2 T}{\partial x^2} + \frac{\partial^2 T}{\partial y^2} \right) + \frac{1}{(\rho_{cp})_{hnf}} (\beta k_r^2) \left(\frac{T}{T_2} \right)^n * \exp \left(\frac{-E_a}{k^* T} \right) (C - C_2) \tag{4}$$

$$\frac{\partial C}{\partial t} + u \frac{\partial C}{\partial x} + v \frac{\partial C}{\partial y} = D \left(\frac{\partial^2 C}{\partial x^2} + \frac{\partial^2 C}{\partial y^2} \right) - k_r^2 \left(\frac{T}{T_2} \right)^n * \exp \left(\frac{-E_a}{k^* T} \right) (C - C_2) \quad (5)$$

where ρ_{hnf} is the density of hybrid nanofluid, σ_e is the electrical conductivity, the B_0^2 magnetic field strength, p is the pressure, k_r^2 the chemical reaction rate constant, E_a activation energy, k^* Boltzmann constant, α_{hnf} is the thermal diffusivity hybrid nanofluid, D is the diffusion co-efficient, ν_{hnf} is the kinematics viscosity of the hybrid nanofluid, and the temperatures are denoted by T_1 . and T_2 , with $T_1 > T_2$. Velocity components are u and v along x and y directions.

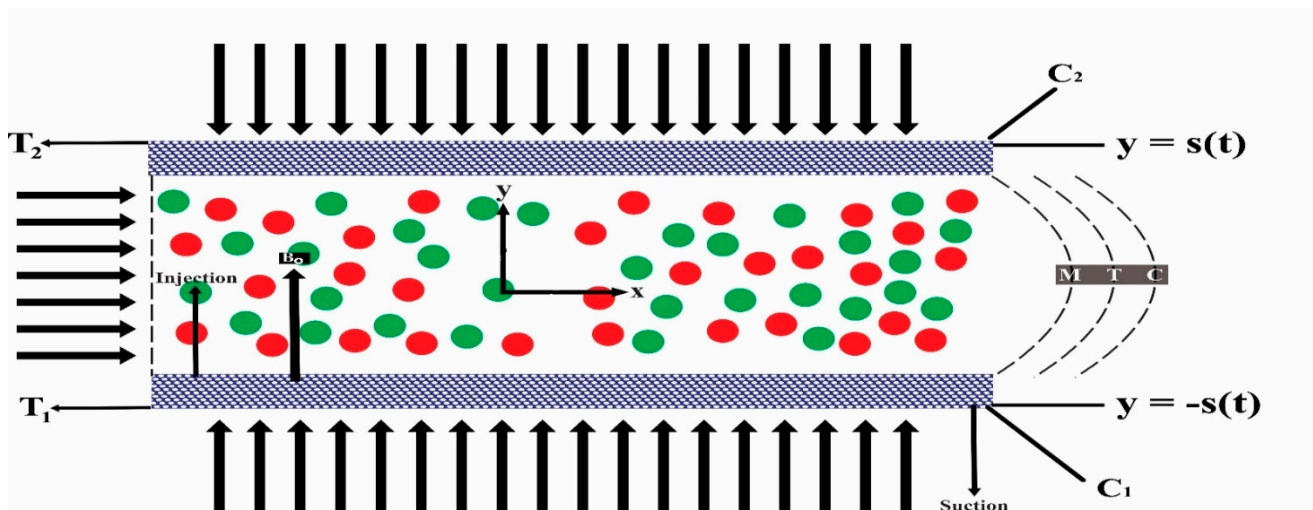


Figure 1. Physical model.

Table 1. Thermo-physical properties of hybrid nanofluids [54].

Properties	Hybrid Nanofluid
Density (ρ)	$\rho_{hnf} = \varphi_1 \rho_{s1} + \varphi_2 \rho_{s2} - (1 - \varphi_1 - \varphi_2) \rho_{bf}$
Viscosity (μ)	$\mu_{hnf} = \frac{\mu_{bf}}{(1 - \varphi_1 - \varphi_2)^{2.5}}$
Heat Capacity $(\rho c_p)_{hnf}$	$\rho c_p hnf = \varphi_1 (\rho c_p) (\rho c_p)_{s1} + \varphi_2 (\rho c_p) (\rho c_p)_{s2} + (1 - \varphi_1 - \varphi_2) (\rho c_p)_{bf}$
Thermal Conductivity (k_{hnf})	$k_{hnf} = \frac{k_{s2} + (N-1)k_{bf} - (N-1)\varphi_2(k_{bf} - k_{s2})}{k_{s2} + (N-1)k_{bf} + \varphi_2(k_{bf} - k_{s2})}$ <p>Where $k_{bf} = \frac{k_{s1} + (N-1)k_f - (N-1)\varphi_1(k_f - k_{s1})}{k_{s1} + (N-1)k_f + \varphi_2(k_f - k_{s1})}$</p>

Table 2. Thermo-physical properties of base fluids and nanoparticles [55].

Title	H ₂ O (f)	TiO ₂	Cu	CuO	Al ₂ O ₃	Ag
ρ (kg m ⁻³)	997.1	4250	8933	3970	6320	10,500
C_p (J kg ⁻¹ k ⁻¹).	4180	686.2	385	765	531.5	235
κ (wm ⁻¹ k ⁻¹)	0.6013	8.9538	401	40	76.5	429

Poor enough temperature variances within the fluid flow allow for a linear expression of the function T^n . By excluding higher-order components, T^n may be enlarged using Taylor’s series concerning temperature T_2 , giving the following approximation:

$$\left. \begin{aligned} T^n &= (1 - n)T_2^n + nT_2^{n-1}T \\ \left(\frac{T}{T_2} \right)^n &= (1 - n) + n \frac{T}{T_2} \end{aligned} \right\} \quad (6)$$

The boundary condition is

$$y = -a(t), u = 0, v = -Aa'(t), T = T_1, C = C_1 \text{ and} \tag{7}$$

$$y = a(t), u = 0, v = Aa'(t), T = T_2, C = C_2$$

$$v_{hnf} = \frac{\mu_{hnf}}{\rho_{hnf}}, \alpha_{hnf} = \frac{k_{hnf}}{(\rho c_p)_{hnf}} \text{ and } Pr = \frac{(\mu C_p)_{bf}}{k_{bf}} \tag{8}$$

where α_{hnf} is the thermal diffusivity of hybrid nanofluid, v_{hnf} is the kinematics viscosity of the hybrid nanofluids, ρ_s and ρ_f are the density for solid and fluid fractions, n is the fitted constant rate, the specific capacitance for hybrid nanofluids is $(\rho c_p)_{hnf}$, and the hybrid nanofluid for the effect of thermal conductivity is k_{hnf} .

The $a'(t)$ represents the derivative $a(t)$ concerning time t and A is the wall permeability factor. We use the following transformation of similarity in the above Equations (2)–(5) after removing the pressure term from the governing equation.

$$\eta = \frac{y}{a}, u = -\frac{xv_f}{a^2} F_\eta(\eta, t), v = \frac{2v_f}{k} F(\eta, t), \theta = \frac{\hat{T} - T_2}{T_1 - T_2}, \chi = \frac{\hat{C} - C_2}{C_1 - C_2} \tag{9}$$

After employing similarity transformation, the continuity Equation (1) is satisfied. However, Equations (2)–(5) are transmuted into the dimensionless form:

$$\frac{v_{hnf}}{v_f} Re f_{\eta\eta\eta\eta} + \alpha(3Re f_{\eta\eta} + \eta Re f_{\eta\eta\eta}) + Re^2 f f_{\eta\eta} - 0 - Re^2 f f_{\eta\eta\eta} - \frac{\rho_f}{\rho_{hnf}} M Re f_{\eta\eta} = 0 \tag{10}$$

$$\theta'' + \frac{k_{bf}}{k_{hnf}} \frac{k_f}{k_{bf}} Pr((1 - \varphi_1 - \varphi_2) + \varphi_1 \frac{(\rho_{cp})_{\rho_1}}{(\rho_{cp})_{hnf}} + \varphi_2 \frac{(\rho_{cp})_{\rho_2}}{(\rho_{cp})_{hnf}})(\eta\alpha - Ref)\theta' - \frac{a^2}{\alpha_{hnf}} \theta_t + (\lambda * \sigma * Pr) \frac{k_{bf}}{k_{hnf}} \frac{k_f}{k_{bf}} (1 + (n * \gamma)\theta[\eta])(1 - E + (E * \gamma)\theta[\eta])\chi[\eta] = 0 \tag{11}$$

$$\chi'' + Sc(\eta\alpha - Ref)\chi' - \frac{a^2}{D} \chi_t + (Sc * \sigma)(1 + (n * \gamma)\theta[\eta])(1 - E + (E * \gamma)\theta[\eta])\chi[\eta] = 0 \tag{12}$$

With the boundary condition

$$F = -Ref, F_\eta = 0, \theta = 1, \chi = 1, \text{ at } \eta = -1$$

$$\text{And, } F = Ref, F_\eta = 0, \theta = 0, \chi = 0, \text{ at } \eta = 1 \tag{13}$$

where $T_1, T_2, C_1,$ and C_2 reflect the temperature of a surface and the concentration of particles at that surface, the lower and upper surfaces' set temperatures, and particle concentrations, respectively; $Pr = \frac{(\mu_{cp})_f}{k_f}, \alpha = \frac{aa'(t)}{v_f}$ is the wall expansion ratio, $Re = \frac{Aaa'(t)}{v_f}$ is the permeability Reynolds number, $\alpha_{hnf} = \frac{k_{hnf}}{(\rho_{cp})_{hnf}}$ thermal diffusivity, $\lambda = \frac{\beta(C_1 - C_2)}{(\rho_{cp})(T_1 - T_2)}$ exothermic/endothermic parameter, $\gamma = \frac{T_1 - T_2}{T_2}$ temperature difference parameter, $\sigma = \frac{k_r(1 - \gamma)}{a}$ dimensionless reaction rate, $M = \frac{\sigma_e B_0^2 a^2}{\mu_f}$ is the magnetic parameter, $E = \frac{E_a}{k^* T}$ dimensional activation energy parameter, and $Sc = \frac{v_f}{D}$ Schmidt Number.

Finally, we set $F = f Re$ and consider the case following Majdalani et al. [56] when α is a constant, $f = f(\eta), \theta = \theta(\eta),$ and $\chi = \chi(\eta),$ which leads to $f_{\eta\eta t} = 0, \theta_t = 0,$ and $\chi_t = 0.$ Thus, we have the following equations, and dividing by Re in the above equation, we get the final result

$$\frac{v_{hnf}}{v_f} f_{\eta\eta\eta\eta} + \alpha(3f_{\eta\eta} + \eta f_{\eta\eta\eta}) - Ref(f_{\eta\eta} - f_{\eta\eta\eta}) - \frac{\rho_f}{\rho_{hnf}} M Re f_{\eta\eta} = 0 \tag{14}$$

$$\theta_{\eta\eta} + \left((1 - (\varphi_1 + \varphi_2)) + (\varphi_1) \left(\frac{\rho_{cps_1}}{\rho_{cpbf}} \right) + (\varphi_2) \left(\frac{\rho_{cps_2}}{\rho_{cpbf}} \right) \right) \left(\frac{k_{bf}}{k_{hnf}} \frac{k_f}{k_{bf}} Pr \right) \alpha \eta - Ref \theta_\eta + (\lambda * \sigma * Pr) \frac{k_{bf}}{k_{hnf}} \frac{k_f}{k_{bf}} (1 + (n * \gamma)\theta[\eta])(1 - E + (E * \gamma)\theta[\eta])\chi[\eta] = 0 \tag{15}$$

$$\chi'' + Sc(\eta\alpha - Ref)\chi' + (Sc * \sigma)(1 + (n * \gamma)\theta[\eta])(1 - E + (E * \gamma)\theta[\eta])\chi[\eta] = 0 \quad (16)$$

$$\begin{aligned} f &= -1, f_\eta = 0, \theta = 1, \chi = 1, \text{ at } \eta = -1, \\ \text{And } f &= 1, f_\eta = 0, \theta = 0, \chi = 0, \text{ at } \eta = 1, \end{aligned} \quad (17)$$

3. Solution Procedure

We use the combination of the ODEs (14), (15), (16), and (17) to solve the boundary value issue numerically. To begin, the boundary value requirements were turned to starting valuation requirements using the “shooting technique” with an adequate initial estimate that fulfilled our parameters, and the problem was then solved using the well-known numerical approach “R–K” method. To obtain the correct findings, the nonlinear system of ODEs was subjected to the Mathematica software. Here, the well-known “shooting iterations technique” has been combined with the well-known Runge–Kutta method. This approach can easily handle the requisite dimensionless ODEs. Using the shooting procedure, we obtain the requisite degree of precision by obtaining the initial condition in such a manner that the constraints are satisfied. First, these ODEs are converted to normal form and rewritten as a first-order system of equations. After establishing adequate start conditions that suited our boundary conditions, the chaotic system of ODES is now prepared for the approved protocol using the Runge–Kutta method.

3.1. Practical and Engineering Interests

Skin friction, the Nusselt number, and the Sherwood numbers are physical parameters that are significant in the engineering goal of modeling equipment at the nanoscale. All of these factors have been estimated on both porous substrates as well.

3.1.1. Skin Friction Coefficients

The C_{f1} and C_{f-1} represent the coefficient of the skin friction of the lower and upper porous surface that is expressed as

$$C_{f-1} = \frac{\zeta_y|_{\eta=-1}}{\rho_f(s'A)^2} = \frac{1}{Re_r(1 - \varphi_1 - \varphi_2)^{2.5}} f''(-1)$$

$$C_{f1} = \frac{\zeta_y|_{\eta=1}}{\rho_f(s'A)^2} = \frac{1}{Re_r(1 - \varphi_1 - \varphi_2)^{2.5}} f''(1)$$

where $Re_r = \left(\frac{\xi}{r}\right) \frac{1}{(Re)^2}$ stands for the local Reynolds number and ζ_y are the shear stresses at the lower and upper plate in the radial direction, respectively,

$$\zeta_y = \mu_{hnf} \left(\frac{\partial u}{\partial y}\right)|_{\eta=-1} = \frac{\mu_{bf}}{(1 - \varphi_1 - \varphi_2)^{2.5}} \left(\frac{rv_f}{s^3}\right) f''(-1)$$

$$\zeta_y = \mu_{hnf} \left(\frac{\partial u}{\partial y}\right)|_{\eta=1} = \frac{\mu_{bf}}{(1 - \varphi_1 - \varphi_2)^{2.5}} \left(\frac{rv_f}{s^3}\right) f''(1)$$

3.1.2. Nusselt Numbers

The calculation at the lower and upper porous surface for the heat transfer rate (Nusselt numbers) Nu_{y-1} and Nu_{y1} are given as

$$Nu_{y-1} = \frac{ad_y}{\kappa_f(T_1 - T_2)}|_{\eta=-1} = -\frac{k_{hnf}}{k_f} \theta'(-1)$$

$$Nu_{y1} = \frac{ad_y}{\kappa_f(T_1 - T_2)}|_{\eta=1} = -\frac{k_{hnf}}{k_f} \theta'(1)$$

Here, heat flux is denoted as d_y , which follows as,

$$d_y|_{\eta=-1} = -k_{hmf} \left(\frac{\partial T}{\partial y} \right) |_{\eta=-1} = -\frac{(T_1 - T_2)}{s} k_{hmf} \theta'(-1)$$

$$d_y|_{\eta=1} = -k_{hmf} \left(\frac{\partial T}{\partial y} \right) |_{\eta=1} = -\frac{(T_1 - T_2)}{s} k_{hmf} \theta'(1)$$

3.1.3. Sherwood Number

The mass transfer rate (Sherwood number) $Sh|_{\eta=-1}$ and $Sh|_{\eta=1}$ at the lower and upper porous surface have the following mathematical expression,

$$Sh|_{\eta=-1} = \frac{aq_z}{D(C_1 - C_2)} |_{\eta=-1} = -\chi'(-1)$$

$$Sh|_{\eta=1} = \frac{aq_z}{D(C_1 - C_2)} |_{\eta=1} = -\chi'(1)$$

where

$$q_z|_{\eta=-1} = -D \left(\frac{\partial C}{\partial y} \right) |_{\eta=-1} = -D \frac{(C_1 - C_2)}{a} \chi'(-1)$$

$$q_z|_{\eta=1} = -D \left(\frac{\partial C}{\partial y} \right) |_{\eta=1} = -D \frac{(C_1 - C_2)}{a} \chi'(1)$$

where $Re = \frac{Aaa'(t)}{v_f}$.

3.1.4. Numerical Solution and Modeling for Thermophysical Properties of (HNfd)

From Equations (14)–(16), convert the nonlinear particles differential equation into a pair of the highly nonlinear coupled system of ordinary differential equations.

$$\left(\frac{1}{(1 - (\varphi_1 + \varphi_2))^{2.5} \left((1 - (\varphi_1 + \varphi_2)) + (\varphi_1) \left(\frac{\rho_{s1}}{\rho_{bf}} \right) + (\varphi_2) \left(\frac{\rho_{s2}}{\rho_{bf}} \right) \right)} \right) f''''[\eta] + \alpha(3f_{\eta\eta} + \eta f_{\eta\eta\eta}) - Re f(f_{\eta\eta} - f_{\eta\eta\eta}) -$$

$$\left(\frac{1}{\left((1 - \varphi_1 - \varphi_2) + \varphi_1 \left(\frac{\rho_{s1}}{\rho_{bf}} \right) + \varphi_2 \left(\frac{\rho_{s2}}{\rho_{bf}} \right) \right)} \right) MRe f_{\eta\eta} = 0 \tag{18}$$

$$\theta''[\eta] + \left((1 - (\varphi_1 + \varphi_2)) + (\varphi_1) \left(\frac{\rho_{cps1}}{\rho_{cpbf}} \right) + (\varphi_2) \left(\frac{\rho_{cps2}}{\rho_{cpbf}} \right) \right)$$

$$\left(\frac{k_{s2} + (N-1)k_{bf} + \varphi_2(k_{bf} - k_{s2})}{k_{s2} + (N-1)k_{bf} - (N-1)\varphi_2(k_{bf} - k_{s2})} \right) \left(\frac{k_{s1} + (N-1)k_f + \varphi_1(k_f - k_{s1})}{k_{s1} + (N-1)k_f - (N-1)\varphi_1(k_f - k_{s1})} \right)$$

$$(Pr(\alpha\eta - Ref[\eta])\theta_\eta) + (\lambda * \sigma * Pr) \left(\frac{k_{s2} + (N-1)k_{bf} + \varphi_2(k_{bf} - k_{s2})}{k_{s2} + (N-1)k_{bf} - (N-1)\varphi_2(k_{bf} - k_{s2})} \right)$$

$$\left(\frac{k_{s1} + (N-1)k_f + \varphi_1(k_f - k_{s1})}{k_{s1} + (N-1)k_f - (N-1)\varphi_1(k_f - k_{s1})} \right) (1 + (n * r)\theta[\eta])(1 - E + (E * r)\theta[\eta])\chi[\eta] = 0. \tag{19}$$

$$\chi'' + Sc(\eta\alpha - Ref)\chi' + (Sc * \sigma)(1 + (n * \gamma)\theta[\eta])(1 - E + (E * \gamma)\theta[\eta])\chi[\eta] = 0 \tag{20}$$

$$H_1 = \left(\frac{1}{(1 - (\varphi_1 + \varphi_2))^{2.5} \left((1 - (\varphi_1 + \varphi_2)) + (\varphi_1) \left(\frac{\rho_{s1}}{\rho_{bf}} \right) + (\varphi_2) \left(\frac{\rho_{s2}}{\rho_{bf}} \right) \right)} \right) \tag{21}$$

$$H_2 = \left(\frac{1}{\left((1 - \varphi_1 - \varphi_2) + \varphi_1 \left(\frac{\rho_{s1}}{\rho_{bf}} \right) + \varphi_2 \left(\frac{\rho_{s2}}{\rho_{bf}} \right) \right)} \right) \tag{22}$$

$$H_3 = \left((1 - (\varphi_1 + \varphi_2)) + (\varphi_1) \left(\frac{\rho_{cps1}}{\rho_{cpbf}} \right) + (\varphi_2) \left(\frac{\rho_{cps2}}{\rho_{cpbf}} \right) \right) \tag{23}$$

$$D_1 = \left(\frac{k_{s2} + (N - 1)k_{mbf} + \varphi_2(k_{mbf} - k_{s2})}{k_{s2} + (N - 1)k_{mbf} - (N - 1)\varphi_2(k_{mbf} - k_{s2})} \right) \tag{24}$$

$$D_2 = \left(\frac{k_{s1} + (N - 1)k_{bf} + \varphi_1(k_{bf} - k_{s1})}{k_{s1} + (N - 1)k_{bf} - (N - 1)\varphi_1(k_{bf} - k_{s1})} \right) \tag{25}$$

$$\omega = D_1 D_2 \tag{26}$$

Putting values of (21), (22), (23), (24), (25), and (26) in Equations (18)–(20), our final results are

$$H_1 f''''[\eta] + \alpha(3f_{\eta\eta} + \eta f_{\eta\eta\eta}) - Ref(f_{\eta\eta} - f_{\eta\eta\eta}) - H_2 MRef_{\eta\eta} = 0 \tag{27}$$

$$\theta''[\eta] + H_3 \omega Pr(\alpha\eta - 2Ref[\eta])\theta'[\eta] + (\lambda * \sigma * Pr)\omega(1 + (n * r)\theta[\eta])(1 - E + (E * r)\theta[\eta])\chi[\eta] = 0 \tag{28}$$

$$\chi'' + Sc(\eta\alpha - Ref)\chi' + (Sc * \sigma)(1 + (n * \gamma)\theta[\eta])(1 - E + (E * \gamma)\theta[\eta])\chi[\eta] = 0 \tag{29}$$

4. Solution of the Problem

We followed the RK methodology with the inclusion of the shooting methods for the purpose of the solution of the existing flow model. The following replacement remains an ingredient to start the process:

$$q_1^* = f[\eta], q_2^* = f'[\eta], q_3^* = f''[\eta], q_4^* = f'''[\eta], q_5^* = \theta[\eta], q_6^* = \theta'[\eta], q_7^* = \chi[\eta], q_8^* = \chi'[\eta] \tag{30}$$

First, transform the model in the following pattern in Equations (27)–(29):

$$f''''[\eta] = \frac{1}{H_1}(-\alpha(3f_{\eta\eta} + \eta f_{\eta\eta\eta}) + Ref(f_{\eta\eta} - f_{\eta\eta\eta}) + H_2 MRef_{\eta\eta}) \tag{31}$$

$$\theta''[\eta] = -(H_3 \omega Pr(\alpha\eta - 2Ref[\eta])\theta'[\eta] + (\lambda * \sigma * Pr)\omega(1 + (n * r)\theta[\eta])(1 - E + (E * r)\theta[\eta])\chi[\eta]) \tag{32}$$

$$\chi''[\eta] = -(Sc(\eta\alpha - Ref)\chi'[\eta] + (Sc * \sigma)(1 + (n * \gamma)\theta[\eta])(1 - E + (E * \gamma)\theta[\eta])\chi[\eta]) \tag{33}$$

By using the substitution, embedded in Equation (30), the following system is attained:

$$\begin{bmatrix} q_1^{*/'} \\ q_2^{*/'} \\ q_3^{*/'} \\ q_4^{*/'} \\ q_5^{*/'} \\ q_6^{*/'} \\ q_7^{*/'} \\ q_8^{*/'} \end{bmatrix} = \begin{bmatrix} q_2^* \\ q_3^* \\ q_4^* \\ \frac{1}{H_1}(-\alpha(3q_3^* + \eta q_4^*) + Re q_1^*(q_3^* - q_4^*) + H_2 MRe q_3^*) \\ q_6^* \\ -(H_3 \omega Pr(\alpha\eta - 2Re q_1^*)q_6^* + (\lambda * \sigma * Pr)\omega(1 + (n * r)q_5^*)(1 - E + (E * r)q_5^*)q_7^*) \\ q_7^* \\ -(Sc(\eta\alpha - Ref)q_7^* + (Sc * \sigma)(1 + (n * \gamma)q_6^*)(1 - E + (E * \gamma)q_6^*)q_8^*) \end{bmatrix} \tag{34}$$

Consequently, the initial condition is:

$$\begin{bmatrix} q_1^* \\ q_2^* \\ q_3^* \\ q_4^* \\ q_5^* \\ q_6^* \\ q_7^* \\ q_8^* \end{bmatrix} = \begin{bmatrix} -1 \\ 0 \\ 1 \\ 0 \\ 1 \\ 0 \\ 1 \\ 0 \end{bmatrix} \tag{35}$$

Now, the above system with the suitable initial condition is solved with help of Mathematics. A well-known Runge–Kutta with shooting technique has been considered to solve the systems of linear equations. The required dimensionless ODEs can easily be tackled with this method. First of all, we obtain the initial condition by using the shooting

technique in such a way that the boundary conditions are satisfied and achieve the desired level of accuracy.

5. Result and Discussion

This section explains the influence of the flow on the concerning equations such as the expansion/contraction ratio parameter, the suction/injection permeable Reynold number, chemical reaction, the activation energy, the magnetic parameter, the Prandtl number, the volume friction parameters, the velocity, temperature, and the concentration profile, as explained through Figures 2–9. In addition, the engineering quantities such as the skin friction coefficients at the upper and lower surface, as well as heat and mass fluxes, are estimated numerically against the variables involved in the presence of the Reynolds number, the expansion ratio, the magnetic field, the Prandtl number, the volume fraction, the exothermic/endothermic parameter, and the reaction rate, as are shown in Tables 3–5. The numerical performance is supported by the competitive contrast. The impacts of the nondimensional variables on the skin friction coefficient are illustrated in Table 3 for various numerical values of the Reynolds number, magnetic parameters, volume friction, and expansion ratio for examining the Newtonian fluid flow. Rises in the values of Re and M significantly improve the magnitudes of both the skin friction coefficients. However, the skin friction coefficient has an inverse relation with the volume of fraction and expansion ratio, and when we raise the values of volume of fraction and expansion ratio, it causes a decrease in the skin friction coefficient for both porous plates. Physically, the Reynolds number is the ratio of the inertial to the viscous forces within a fluid that is subjected to relative internal movement as a result of fluctuating fluid velocities. Table 4 accentuates the variation of the heat and mass transfer for the different values of Re , M , γ , σ , α , φ_1 , φ_2 , n . The values of Re are greater than zero, and the flow rate of heat and mass transfer is enhanced; furthermore, the M , α , φ_1 , φ_2 parameters are increased and the flow of thermal and the mass fluid rate is reduced in both circumstances. It is observed that by increasing magnetic parameter values, the flow of heat transfer rate decreases. This is because by enhancing the magnetic value, Lorentz forces are produced, decreasing the axial momentum of the fluid particles. We can conclude from this argument that the transverse application magnetic field normalizes the fluid velocity. The magnetic effect causes the particles within the fluid to vibrate, which is governed by the Lorentz force. Moreover, when we enhance the value of the dimensionless activation energy parameter (E), the similarity variable (n), the temperature difference parameter (γ), and the dimensionless reaction rate (σ), then the flow of the hybrid nanofluids are effective in the opposite. The results in Table 5 show that the flow of the heat transfer depends on the Prandtl number and the dimensionless exothermic/endothermic parameter in such a way that, when we increase the value of these parameters, it causes enhance in the heat transfer for both porous surfaces. Table 6 shows the volume of the fraction effect on a Nusselt number for different types of nanofluids and hybrid nanofluids. If we increased the value of both volume fractions φ_1 and φ_2 , then we analyzed that the hybrid nanofluid (Ag – CuO/H₂O) had much better thermal conductivity values of the Nusselt number than the other different combinations such as the nanofluids and hybrid nanofluids. Table 7 shows the comparison results of the heat transfer rate of the present work and AHMAD et al. [57]. Figure 2 is plotted to show the behavior of the expansion/contraction parameter onto the thermal profile. It is noticed that as the value of α_* increases, the heat transfer rate is reduced at the upper disk and increases at the lower disk. Figure 3 demonstrated the impact of the expansion ratio on the mass concentration profile. If the expansion ratio varies from $-ve$ to $+ve$ values, then the mass concentration boundary layer thickness increases in the lower wall but gradually decreases in the upper wall. Figure 4 shows that by enhancing the values of the expansion ratio parameter, the middle of the wall's momentum boundary layer flow turns very high, and the flow behavior of fluid is graphically symmetrical in the velocity profile. While Figure 5 reflects the dimensionless activation energy parameter on the temperature profiles $\theta(\eta)$ for the fixed value of $a = -2$, $Re = -0.5$, $Pr = 6.2$, it shows

that the fluid’s temperature reduces as E increases. In an endothermic reaction, the number of extremely energetic particles with energies equal to (or higher than) the activation energy increases as E grows. This results in a decrease in the fluid temperature. Falls also occur in the upper and lower thermal boundary layers in certain circumstances. In the same way, increasing the dimensionless activation energy parameter E on the mass profiles induces a decline in the upper and lower boundary layer, as shown in Figure 6. According to Figure 7, the effect of the Schmidt number on the concentration profiles $\chi(\eta)$ for the fixed $a = 3$, $Pr = 6.2$, $\gamma = 0.1$ is just like when we expand the Schmidt number, which then fall occurs in its upper boundary layer, and growth occurs in the lower boundary layer. The ratio of the momentum diffusivity (kinematic viscosity) to mass diffusivity is defined as the Schmidt number (Sc). It is used to describe fluid flows that have both momentum and mass diffusion convection going on at the same time. In Figure 8, we observed the effect on the radical velocity profile, where the middle of the wall results is enlarged just by enlarging the effect of the volume of a fraction on radical velocity profiles. Figure 9 is related to the volume fraction effect on temperature profile, having a scale from 0.1 to 0.5; as a result, its upper boundary layer falls and the lower boundary layer increases.

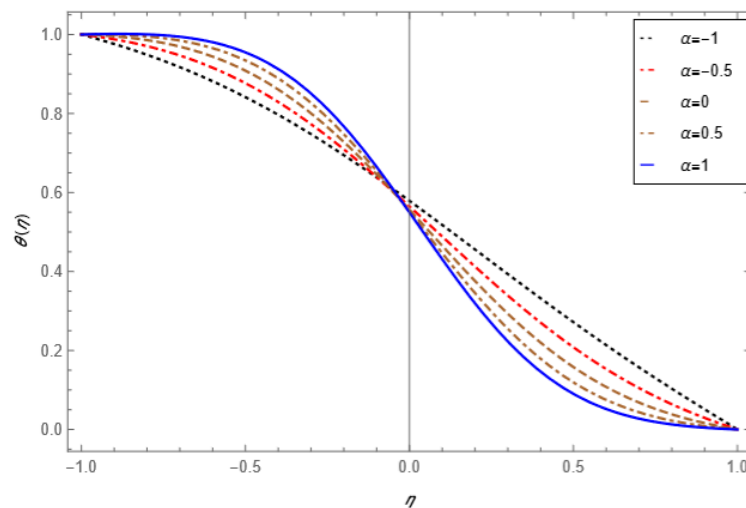


Figure 2. Expansion ratio effect on a temperature profile for $\varphi_1 = \varphi_2 = 0.01$, $Pr = 6.2$, $\sigma = 0.1$.

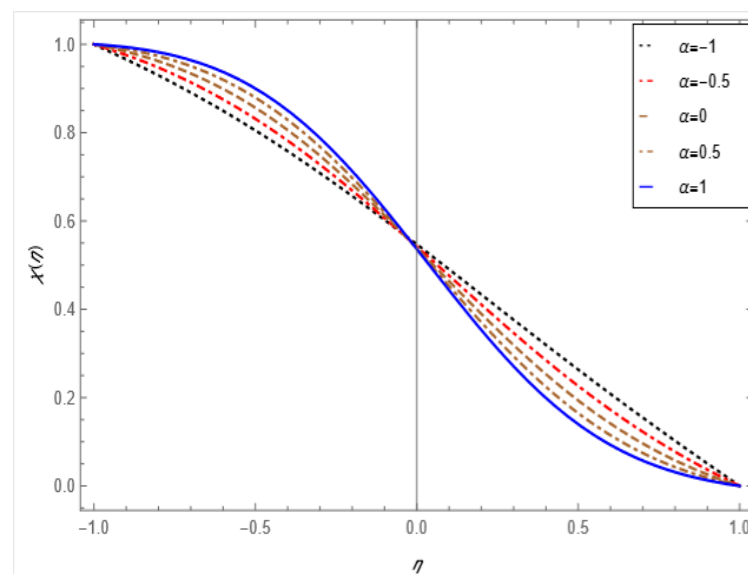


Figure 3. Expansion ratio effect on a concentration profile for $Re = -1$, $\varphi_1 = \varphi_2 = 0.01$, $Sc = 1$.

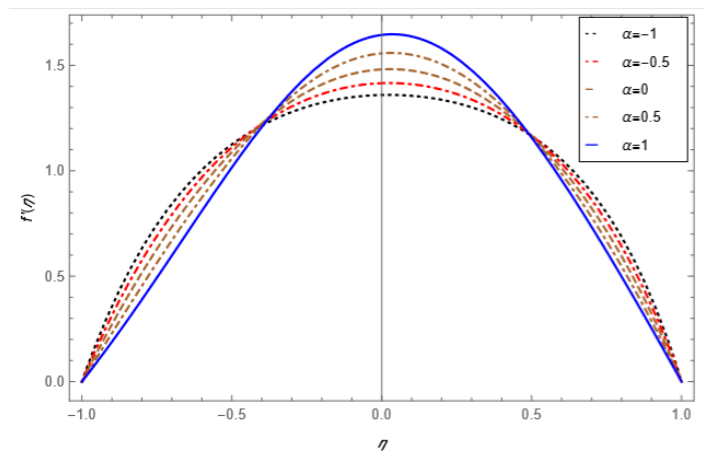


Figure 4. Expansion ratio effect on the velocity for $R_e = -1$, $\phi_1 = \phi_2 = 0.01$, $M = 1$.

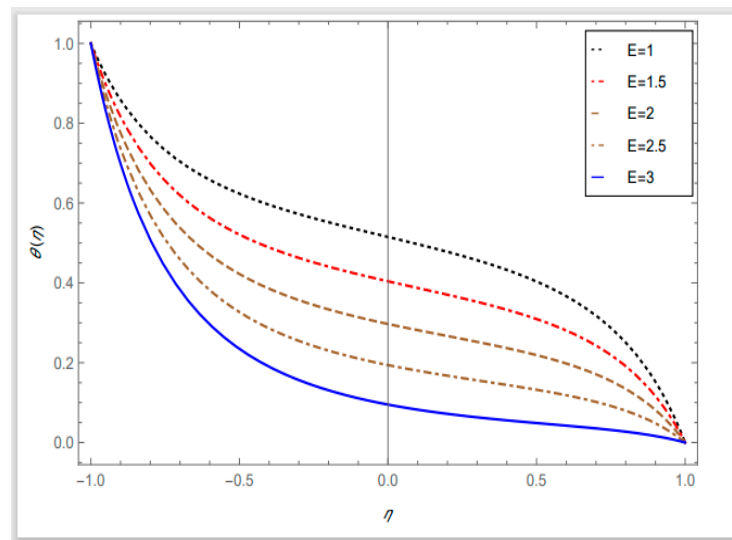


Figure 5. Dimensionless activation energy parameter on the temperature profile at $a = -2$, $R_e = -0.5$, $Sc = 1$.

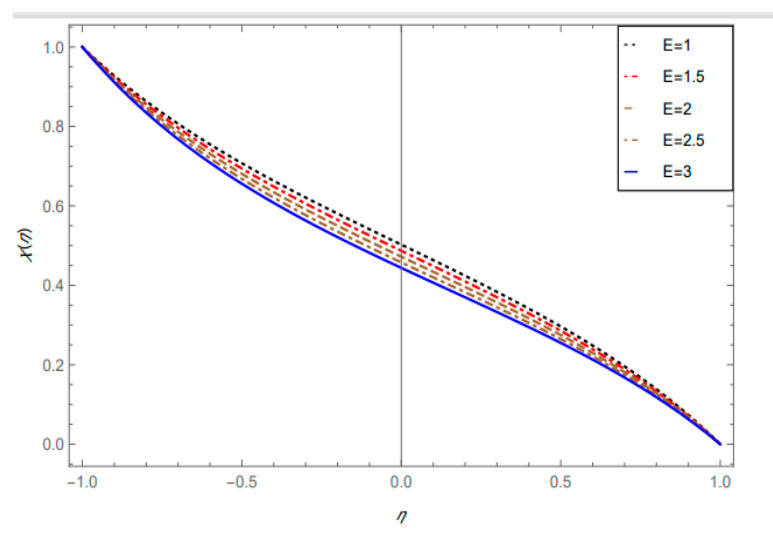


Figure 6. Dimensionless activation energy parameter effect on the concentration profile at $a = -2$, $R_e = -0.5$, $Pr = 6.2$.

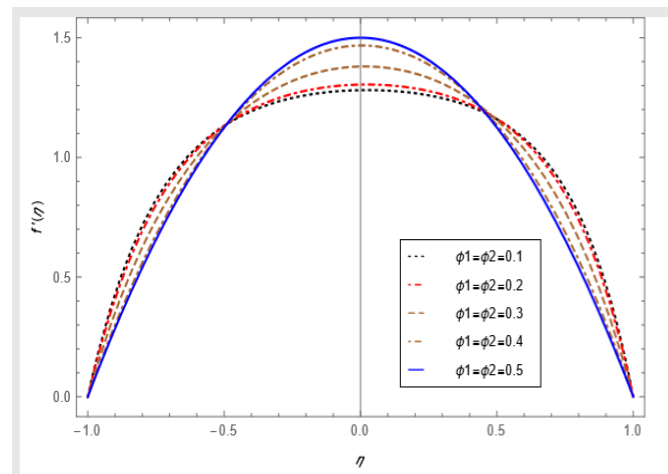


Figure 7. Volume fraction effect on the radical velocity profile at $a = -2, R_e = -1, M = 1$.

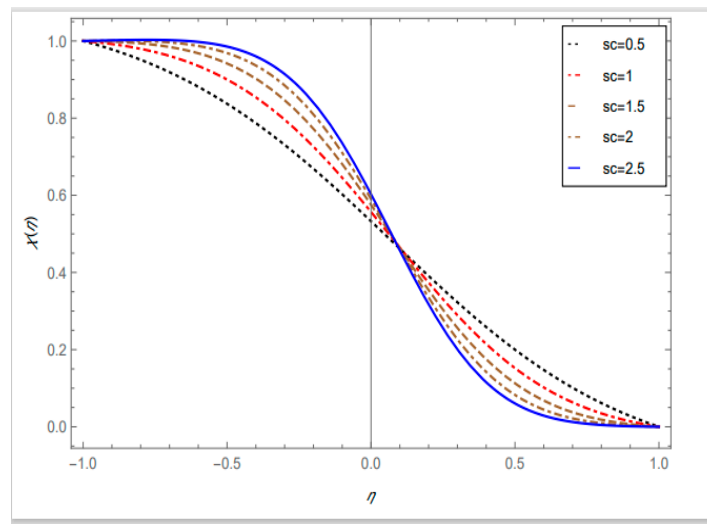


Figure 8. Schmidt number effect on the concentration profile at $a = 3, Pr = 6.2, \phi = 0.1$.

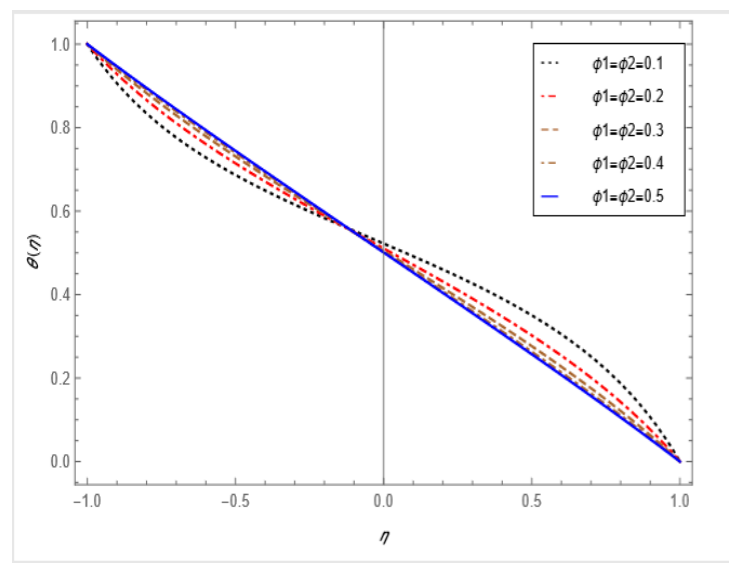


Figure 9. Volume fraction effect on the temperature profile $a = -2, Pr = 6.2, R_e = -1$.

Table 3. Calculation of the effects of flow on the skin friction coefficient from upper and lower porous surfaces.

Re	M	φ_1	φ_2	α	$ C_{f-1} $	$ C_{f1} $
1	1	0.01	0.01	1	3.1951	3.1951
1.2					3.3435	3.3435
1.4					3.4983	3.4983
	1				2.0561	2.0561
	3				2.0954	2.0954
	5				2.1342	2.1342
		0.01			2.0561	2.0561
		0.03			1.8766	1.8766
		0.05			1.7305	1.7305
			0.03		1.9986	1.9986
			0.06		1.9306	1.9306
			0.09		1.8815	1.8815
				0.1	2.3866	2.3866
				0.5	2.0561	2.0561
				0.9	1.7391	1.7391

Table 4. Impact of flow heat and mass transfer for different nondimensional parameter values such as the Reynolds number, magnetic parameter, volume of fraction, expansion ratio, and E, n, γ, σ .

Re	M	φ_1	φ_2	α	E	n	γ	σ	$ \theta(-1) $	$ \chi(-1) $
1	1	0.01	0.01	1	0.5	1	0.1	0.1	0.03404	0.54716
1.2									0.65331	0.58341
1.4									2.31701	0.61933
	1								0.05014	0.23003
	3								0.05011	0.23028
	5								0.05007	0.23053
		0.01							0.05014	0.23003
		0.03							0.04852	0.22816
		0.05							0.04646	0.22648
			0.03						0.04822	0.22941
			0.06						0.04445	0.22871
			0.09						0.03947	0.22821
				0.1					0.05491	0.27063
				0.5					0.05014	0.23003
				0.9					0.04317	0.19439
					0.2				0.05014	0.23003
					0.5				0.03128	0.24244
					0.8				0.01247	0.25476
						0.35			0.05156	0.22917
						0.70			0.05355	0.22797
						0.95			0.05497	0.22711

Table 4. Cont.

<i>Re</i>	<i>M</i>	φ_1	φ_2	α	<i>E</i>	<i>n</i>	γ	σ	$ \theta(-1) $	$ \chi(-1) $
							0.15		0.05112	0.22943
							0.20		0.05212	0.22883
							0.25		0.06641	0.22016
								0.20	0.10771	0.26723
								0.50	0.28441	0.24433
								0.80	0.51531	0.22101

Table 5. Numerical effect of heat transfer on the Prandtl number and dimensionless exothermic/endothermic parameter.

<i>Pr</i>	λ	$ \theta(-1) $	$ \theta(1) $
5.0	6.2	0.03991	0.03991
5.5		0.04536	0.04536
6.2		0.05414	0.05414
	1.3	0.06720	0.06720
	1.5	0.07869	0.07869
	1.7	0.09884	0.09884

Table 6. Impact on the Nusselt number in volume fraction for nanofluids and trihybrid nanofluids.

$\varphi_1 = \varphi_2$	<i>Cu/H₂O</i> $ Nu_{y1} $	<i>Ag/H₂O</i> $ Nu_{y1} $	<i>Al₂O₃/H₂O</i> $ Nu_{y1} $	<i>CuO/H₂O</i> $ Nu_{y1} $	<i>TiO₂/H₂O</i> $ Nu_{y1} $	<i>Cu–TiO₂/H₂O</i> $ Nu_{y1} $	<i>Cu–Al₂O₃/H₂O</i> $ Nu_{y1} $	<i>Ag–CuO/H₂O</i> $ Nu_{y1} $
0.01 = 1%	0.05680	0.05725	0.05703	0.05680	0.05532	0.07364	0.07432	0.07620
0.03 = 3%	0.07621	0.07712	0.07651	0.07585	0.07158	0.09113	0.09332	0.09913
0.05 = 5%	0.09524	0.09616	0.09520	0.09415	0.08734	0.10984	0.11366	0.12315
0.07 = 7%	0.11368	0.11440	0.11310	0.11172	0.01025	0.12983	0.13531	0.14771
0.09 = 9%	0.13152	0.13187	0.13023	0.12858	0.11733	0.15099	0.15802	0.17231

Table 7. Comparison results in the skin friction coefficient at the lower plate for *Re* = 0, γ = 0, σ = 0, λ = 0, *M* = 0, *E* = 0, *n* = 0.

<i>Sc</i>	<i>Pr</i>	AHMAD et al. [57]	Present Results
		$Re_r C_{f-1}$	$Re_r C_{f-1}$
1.1	2	1.17039	1.17040
1.2		1.27024	1.27025
1.4		1.36100	1.36101
1.6		1.41025	1.41026
1.1	2	1.17039	1.17040
	1.5	1.10472	1.10474
	1	1.01015	1.01017
	0.5	0.82109	0.82110

6. Numerical Stability

The missing initial condition at the beginning of the interval is assumed in a shooting approach, and the differential equation is then numerically integrated as an initial value

issue. Then, by comparing the computed value of the dependent variable at the terminal point to the value given here, the accuracy of the ostensibly absent initial condition is confirmed. If there is a discrepancy, the procedure must be repeated with a new value for the missing beginning condition. This procedure is continued until all of the calculated and given conditions agree. The uniformity of our simulation solution as the step-size decreases is seen in Table 8 (below), providing us assurance in our computing technique. At the bottom wall, our design parameters produce symmetric and precise shear stress results.

Table 8. Numerical stability of outcomes at various values of η .

η	$f(-1)$	$f'(-1)$	$f''(-1)$
−1	−1	0	2.8682185248890812
−0.9	−0.986004632148899	0.2762900573162856	2.6513635499005477
−0.8	−0.9455224728264963	0.5291984277529419	2.4022339523123413
−0.7	−0.8810372014384086	0.7559667541088714	2.129942115638948
−0.6	−0.7952655915371383	0.9546625435491819	1.8418610445096326
−0.5	−0.6910837969233515	1.1240010434185939	1.5435889317798919
−0.4	−0.5714712122097215	1.263175625521357	1.2391316972955884
−0.3	−0.4394701755700228	1.371712201118385	0.93118511715582
−0.2	−0.29815875720869417	1.4493534762608988	0.6214396059796121
−0.1	−0.1506336107568336	1.4959731677879262	0.31087067312291067
0	$1.55484340680353 \times 10^{-10}$	1.5115177949361303	$1.2913497632327 \times 10^{-9}$
0.1	0.1506336107568336	1.4959731683236508	0.31087067312291067
0.2	0.29815875720869417	1.4493534762608988	0.6214396059796121
0.3	0.4394701755700228	1.371712201118385	0.93118511715582
0.4	0.5714712122097215	1.263175625521357	1.2391316972955884
0.5	0.6910837969233515	1.1240010434185939	1.5435889317798919
0.6	0.7952655915371383	0.9546625435491819	1.8418610445096326
0.7	0.8810372014384086	0.7559667541088714	2.129942115638948
0.8	0.9455224728264963	0.5291984277529419	2.4022339523123413
0.9	0.986004632148899	0.5291984277529419	2.6513635499005477
1	1	0	2.8682185248890812

7. Conclusions

We investigated the heat and mass transport properties of magnetized hybrid nanofluids flowing across movable plates through porous surfaces with activation energy and chemical reaction effects in this research. We used six different forms of NPS for this purpose. Taking water as a base fluid for metallic and metallic oxides, consequences are achieved in terms of numbers and graphs. Furthermore, we infer that the thermal conductivity of hybrid nanofluid outperforms simple nanofluid in terms of performance. The following are the most important findings:

- The skin friction coefficient increases at both porous walls with the increase in the permeable Reynolds number, and a similar trend is observed for the nanoparticles volume fraction.
- The Nusselt number shows significant results under the effect of the hybrid nanofluid Ag – CuO/H₂O flow.
- The Prandtl number Pr has a significant role in the heat transfer system for every type of hybrid nanofluid flow.
- When the dimensionless activation energy parameter has higher values, the rate of the mass transfer rises.
- The measurements of the dimensionless exothermic/endothermic parameter and the dimensionless reaction rate parameter are increased; the flow of heat transfer improves progressively.
- As the values of the Schmidt number rise, the mass transfer flow improves on the lower porous surfaces.
- For the injection cases, the hybrid nanoparticles have a significant effect on the temperature as well as the radial velocity.

After the successful numerical computation of the present study, this fluid model may be extended for Casson hybrid nanofluid, Maxwell hybrid nanofluid, and Oldroyd-B hybrid nanofluid. This numerical computation is relevant to heat exchangers, polymers, astrophysical and geophysical problems, and biomedicine.

Author Contributions: Investigation, B.A.K.; Methodology, M.Z.A.Q.; Software, A.K.H.; Supervision, J.D.C.; Validation, B.A.; Writing—original draft, Q.R. and B.A.; Writing—review & editing, N.A.S. and J.D.C. All authors have read and agreed to the published version of the manuscript.

Funding: This research received no external funding.

Institutional Review Board Statement: Not Applicable.

Informed Consent Statement: Not Applicable.

Data Availability Statement: The numerical data used to support the findings of this study are included within the article.

Acknowledgments: This work was supported by the Technology Innovation Program (20018869, Development of Waste Heat and Waste Cold Recovery Bus Air-conditioning System to Reduce Heating and Cooling Load by 10%) funded By the Ministry of Trade, Industry & Energy (MOTIE, Korea).

Conflicts of Interest: The authors declare no conflict of interest.

Nomenclature

u, v	Velocity components
Sc	Schmidt number
T	Temperature
$(C_p)_{hnf}$	Hybrid nanofluids specific heat
α	Expansion ratio
E	Dimensionless activation energy Parameter
E_a	Activation energy
C_1	Lower plate concentration
T_2	Upper plate temperature
B_0	Magnetic field strength
φ_1, φ_2	Nanoparticles volume fraction
ρ_{bf}	Water density (base fluid)
ρ_{s1}, ρ_{s2}	Density for nanoparticles 1st and 2nd
k	Thermal conductivity
k_{s1}, k_{s2}	Thermal conductivity for nanoparticles 1st and 2nd
M	Magnetic field
k^*	Boltzmann constant
β	Exothermic/endothermic coefficient
Pr	Prandtl number
n	Dimensionless parameter
Re	Reynolds number
N	Size
λ	Dimensionless exothermic/endothermic Parameter
σ	Dimensionless reaction rate
T_1	Lower plate temperature
C_2	Upper plate concentration
γ_1	Temperature difference parameter
x, y	Space coordinate
ρ_{hnf}	Hybrid nanofluids density
k_{hnf}	Hybrid nanofluid's thermal conductivity
μ_f	Water dynamic velocity
B_{fd}	Base fluid

α_{hmf}	Thermal diffusivity hybrid Nanofluid
N	Similarity variable
D	Diffusion coefficient

References

- Sreedevi, P.; Reddy, P.S.; Chamkha, A. Heat and mass transfer analysis of unsteady hybrid nanofluid flow over a stretching sheet with thermal radiation. *SN Appl. Sci.* **2020**, *2*, 1222. [[CrossRef](#)]
- Roy, N.C.; Pop, I. Heat and mass transfer of a hybrid nanofluid flow with binary chemical reaction over a permeable shrinking surface. *Chin. J. Phys.* **2021**, *76*, 283–298. [[CrossRef](#)]
- Xu, H. Modelling unsteady mixed convection of a nanofluid suspended with multiple kinds of nanoparticles between two rotating disks by generalized hybrid model. *Int. Commun. Heat Mass Transf.* **2019**, *108*, 104275. [[CrossRef](#)]
- Kapen, P.T.; Ketchate, C.G.N.; Fokwa, D.; Tchuen, G. Linear stability analysis of (Cu-Al₂O₃)/water hybrid nanofluid flow in porous media in presence of hydromagnetic, small suction and injection effects. *Alex. Eng. J.* **2021**, *60*, 1525–1536. [[CrossRef](#)]
- Maskeen, M.M.; Zeeshan, A.; Mehmood, O.U.; Hassan, M. Heat transfer enhancement in hydromagnetic alumina–copper/water hybrid nanofluid flow over a stretching cylinder. *J. Therm. Anal.* **2019**, *138*, 1127–1136. [[CrossRef](#)]
- Devi, S.S.U.; Devi, S.P.A. Numerical investigation of three-dimensional hybrid Cu–Al₂O₃/Water nanofluids flow over a stretching sheet with effecting Lorentz force subject to Newtonian heating. *Can. J. Phys.* **2016**, *94*, 490–496. [[CrossRef](#)]
- Sahoo, R.R.; Kumar, V. Development of a new correlation to determine the viscosity of ternary hybrid nanofluids. *Int. Commun. Heat Mass Transf.* **2020**, *111*, 104451. [[CrossRef](#)]
- Aladdin, N.A.L.; Bachok, N.; Pop, I. Cu–Al₂O₃/water hybrid nanofluids flow over a permeable moving surface in presence of hydromagnetic and suction effects. *Alex. Eng. J.* **2020**, *59*, 657–666. [[CrossRef](#)]
- Waini, I.; Ishak, A.; Pop, I. Hybrid nanofluid flow and heat transfer over a nonlinear permeable stretching/shrinking surface. *Int. J. Numer. Methods Heat Fluid Flow* **2019**, *29*, 3110–3127. [[CrossRef](#)]
- Hayat, T.; Nadeem, S. Heat transfer enhancement with Ag–CuO/water hybrid nanofluids. *Results Phys.* **2017**, *7*, 2317–2324. [[CrossRef](#)]
- Das, P.K. A review based on the effect and mechanism of thermal conductivity of normal nanofluids and hybrid nanofluids. *J. Mol. Liq.* **2017**, *240*, 420–446. [[CrossRef](#)]
- Zainal, N.A.; Nazar, R.; Naganthran, K.; Pop, I. MHD flow and heat transfer of hybrid nanofluids over a permeable moving surface in the presence of thermal radiation. *Int. J. Numer. Methods Heat Fluid Flow* **2020**, *31*, 858–879. [[CrossRef](#)]
- Devi, S.U.; Devi, S.P.A. Heat transfer enhancement of CuAl₂O₃/water hybrid nanofluids flow over a stretching sheet. *J. Niger. Math. Soc.* **2017**, *36*, 419–433.
- Chahregh, H.S.; Dinarvand, S. TiO₂–Ag/blood hybrid nanofluids flow through an artery with applications of drug delivery and blood circulation in the respiratory system. *Int. J. Numer. Methods Heat Fluid Flow* **2020**, *11*, 4775–4796. [[CrossRef](#)]
- Dinarvand, S.; Nademi Rostami MDinarvand, R.; Pop, I. Improvement of drug delivery micro-circulatory system with a novel pattern of CuO–Cu/blood hybrid nanofluids flow towards a porous stretching sheet. *Int. J. Numer. Methods Heat Fluid Flow* **2019**, *29*, 4408–4429. [[CrossRef](#)]
- Shahsavari, A.; Talebizadeh Sardari, P.; Toghraie, D. Free convection heat transfer and entropy generation analysis of water–Fe₃O₄/CNT hybrid nanofluids in a concentric annulus. *Int. J. Numer. Methods Heat Fluid Flow* **2019**, *29*, 915–934. [[CrossRef](#)]
- Ahamed, N.; Asirvatham, L.G.; Wong, W.S. Entropy generation analysis of graphene–alumina hybrid nanofluid in multipoint mini-channel heat exchanger coupled with thermoelectric cooler. *Int. J. Heat Mass Transf.* **2016**, *103*, 1084–1097. [[CrossRef](#)]
- Chamkha, A.J.; Dogonchi, A.S.; Ganji, D.D. Magneto-hydrodynamic flow and heat transfer of a hybrid nanofluids in a rotating system among two surfaces in the presence of thermal radiation and Joule heating. *AIP Adv.* **2019**, *9*, 025103. [[CrossRef](#)]
- Bhattad, A.; Sarkar, J.; Ghosh, P. Discrete phase numerical model and experimental study of hybrid nanofluid heat transfer and pressure drop in plate heat exchanger. *Int. Commun. Heat Mass Transf.* **2018**, *91*, 262–273. [[CrossRef](#)]
- Hussien, A.A.; Abdullah, M.Z.; Yusop, N.M.; Al-Nimr, M.A.; Atieh, M.A.; Mehrali, M. Experiment on forced convective heat transfer enhancement using MWCNTs/GNPs hybrid nanofluid and monotube. *Int. J. Heat Mass Transf.* **2017**, *115*, 1121–1131. [[CrossRef](#)]
- Soltani, O.; Akbari, M. Effects of temperature and particles concentration on the dynamic viscosity of MgO–MWCNT/ethylene glycol hybrid nanofluids: Experimental study. *Phys. E* **2016**, *84*, 564–570. [[CrossRef](#)]
- Abdelmalek, Z.; Qureshi, M.Z.A.; Bilal, S.; Raza, Q.; Sherif, E.-S.M. A case study on morphological aspects of distinct magnetized 3D hybrid nanoparticles on fluid flow between two orthogonal rotating disks: An application of thermal energy systems. *Case Stud. Therm. Eng.* **2020**, *23*, 100744. [[CrossRef](#)]
- Singh, K.; Kumar, M. Influence of Chemical Reaction on Heat and Mass Transfer Flow of a Micropolar Fluid over a Permeable Channel with Radiation and Heat Generation. *J. Thermodyn.* **2016**, *2016*, 8307980. [[CrossRef](#)]
- Ojjela, O.; Kumar, N.N. Unsteady Heat and Mass Transfer of Chemically Reacting Micropolar Fluid in a Porous Channel with Hall and Ion Slip Currents. *Int. Sch. Res. Not.* **2014**, *2014*, 646957. [[CrossRef](#)] [[PubMed](#)]
- Roy, N.C.; Pop, I. Analytical investigation of transient free convection and heat transfer of a hybrid nanofluid between two vertical parallel plates. *Phys. Fluids* **2022**, *34*, 072005. [[CrossRef](#)]

26. Jyothi, A.M.; Kumar, R.S.V.; Madhukesh, J.K.; Prasannakumara, B.C.; Ramesh, G.K. Squeezing flow of Casson hybrid nanofluid between parallel plates with a heat source or sink and thermophoretic particle deposition. *Heat Transf.* **2021**, *50*, 7139–7156. [[CrossRef](#)]
27. Santhi, M.; Rao, K.V.S.; Reddy, P.S.; Sreedevi, P. Heat and mass transfer characteristics of radiative hybrid nanofluid flow over a stretching sheet with chemical reaction. *Heat Transf.* **2020**, *50*, 2929–2949. [[CrossRef](#)]
28. Bilal, M.; Gul, T.; Alsubie, A.; Ali, I. Axisymmetric hybrid nanofluid flow with heat and mass transfer amongst the two gyrating plates. *ZAMM-J. Appl. Math. Mech. Z. Für Angew. Math. Und Mech.* **2021**, *101*, e202000146. [[CrossRef](#)]
29. Ramesh, G.K.; Madhukesh, J.K.; Prasannakumara, B.C.; Roopa, G.S. Significance of aluminium alloys particle flow through a parallel plates with activation energy and chemical reaction. *J. Therm. Anal.* **2021**, *147*, 6971–6981. [[CrossRef](#)]
30. Shanmugapriya, M.; Sundareswaran, R.; Kumar, P.S. Heat and Mass Transfer Enhancement of MHD Hybrid Nanofluid Flow in the Presence of Activation Energy. *Int. J. Chem. Eng.* **2021**, *2021*, 9473226. [[CrossRef](#)]
31. Shah, N.A.; Wakif, A.; El-Zahar, E.R.; Ahmad, S.; Yook, S.-J. Numerical simulation of a thermally enhanced EMHD flow of a heterogeneous micropolar mixture comprising (60%)-ethylene glycol (EG), (40%)-water (W), and copper oxide nanomaterials (CuO). *Case Stud. Therm. Eng.* **2022**, *35*, 102046. [[CrossRef](#)]
32. Ali, B.; Naqvi, R.A.; Ali, L.; Abdal, S.; Hussain, S. A comparative description on time-dependent rotating magnetic transport of a water base liquid H₂O with hybrid nano-materials Al₂O₃-Cu and Al₂O₃-TiO₂ over an extending sheet using Buongiorno model: Finite element approach. *Chin. J. Phys.* **2021**, *70*, 125–139. [[CrossRef](#)]
33. Ali, B.; Khan, S.A.; Hussein, A.K.; Thumma, T.; Hussain, S. Hybrid nanofluids: Significance of gravity modulation, heat source/sink, and magnetohydrodynamic on dynamics of micropolar fluid over an inclined surface via finite element simulation. *Appl. Math. Comput.* **2021**, *419*, 126878. [[CrossRef](#)]
34. Sajjan, K.; Shah, N.A.; Ahammad, N.A.; Raju, C.S.K.; Kumar, M.D.; Weera, W. Nonlinear Boussinesq and Rosseland approximations on 3D flow in an interruption of Ternary nanoparticles with various shapes of densities and conductivity properties. *AIMS Mathematics* **2022**, *7*, 18416–18449. [[CrossRef](#)]
35. Bestman, A.R. Natural convection boundary layer with suction and mass transfer in a porous medium. *Int. J. Energy Res.* **1990**, *14*, 389–396. [[CrossRef](#)]
36. Khan, N.S.; Kumam, P.; Thounthong, P. Second law analysis with effects of Arrhenius activation energy and binary chemical reaction on nanofluids flow. *Sci. Rep.* **2020**, *10*, 1226. [[CrossRef](#)]
37. Jayadevamurthy, P.G.R.; Rangaswamy, N.K.; Prasanna kumara, B.C.; Nisar, K.S. Emphasis on unsteady dynamics of bioconvective hybrid nanofluids flow over an upward–downward moving rotating disk. *Numer. Methods Partial. Differ. Equ.* **2020**, *5*, 1–22. [[CrossRef](#)]
38. Reddy, M.G.; Naveen, K.R.; Prasanna, K.B.; Rudraswamy, N.G.; Kumar, K.G. Magnetohydrodynamic flow and heat transfer of a hybrid nanofluids over a rotating disk by considering Arrhenius energy. *Commun. Theor. Phys.* **2021**, *73*, 045002. [[CrossRef](#)]
39. Mustafa, M.; Khan, J.A.; Hayat, T.; Alsaedi, A. Buoyancy effects on the MHD nanofluids flow past a vertical surface with chemical Reaction and activation energy. *Int. J. Heat Mass Transf.* **2017**, *108*, 1340–1346. [[CrossRef](#)]
40. Bhatti, M.M.; Michaelides, E.E. Study of Arrhenius activation energy on the thermo-bioconvection nanofluid flow over a Riga plate. *J. Anal. Calorim.* **2020**, *143*, 2029–2038. [[CrossRef](#)]
41. Kasaeian, A.; Daneshazarian, R.; Mahian, O.; Kolsi, L.; Chamkha, A.J.; Wongwises, S.; Pop, I. Nanofluid flow and heat transfer in porous media: A review of the latest developments. *Int. J. Heat Mass Transf.* **2017**, *107*, 778–791. [[CrossRef](#)]
42. Singh, J.; Mahabaleshwar, U.S.; Bognár, G. Mass Transpiration in Nonlinear MHD Flow Due to Porous Stretching Sheet. *Sci. Rep.* **2019**, *9*, 18484. [[CrossRef](#)] [[PubMed](#)]
43. Subhani, M.; Nadeem, S. Numerical investigation into unsteady magnetohydrodynamics flow of micropolar hybrid nanofluid in porous medium. *Phys. Scr.* **2019**, *94*, 105–120. [[CrossRef](#)]
44. Al-Zamily, A.M.J. Analysis of natural convection and entropy generation in a cavity filled with multi-layers of porous medium and nanofluids with a heat generation. *Int. J. Heat Mass Transf.* **2017**, *106*, 1218–1231. [[CrossRef](#)]
45. Dzulkifli, N.F.; Bachok, N.; Yacob, N.A.; Arifin, N.; Rosali, H. Unsteady Stagnation-Point Flow and Heat Transfer Over a Permeable Exponential Stretching/Shrinking Sheet in Nanofluid with Slip Velocity Effect: A Stability Analysis. *Appl. Sci.* **2018**, *8*, 2172. [[CrossRef](#)]
46. Younis, O.; Alizadeh, M.; Hussein, A.K.; Ali, B.; Biswal, U.; Malekshah, E.H. MHD Natural Convection and Radiation over a Flame in a Partially Heated Semicircular Cavity Filled with a Nanofluid. *Mathematics* **2022**, *10*, 1347. [[CrossRef](#)]
47. Lou, Q.; Ali, B.; Rehman, S.U.; Habib, D.; Abdal, S.; Shah, N.A.; Chung, J.D. Micropolar Dusty Fluid: Coriolis Force Effects on Dynamics of MHD Rotating Fluid When Lorentz Force Is Significant. *Mathematics* **2022**, *10*, 2630. [[CrossRef](#)]
48. Ashraf, M.Z.; Rehman, S.U.; Farid, S.; Hussein, A.K.; Ali, B.; Shah, N.A.; Weera, W. Insight into Significance of Bioconvection on MHD Tangent Hyperbolic Nanofluid Flow of Irregular Thickness across a Slender Elastic Surface. *Mathematics* **2022**, *10*, 2592. [[CrossRef](#)]
49. Mehryan, S.; Sheremet, M.A.; Soltani, M.; Izadi, M. Natural convection of magnetic hybrid nanofluid inside a double-porous medium using two-equation energy model. *J. Mol. Liq.* **2019**, *277*, 959–970. [[CrossRef](#)]
50. Mallikarjuna, B.; Rashad, A.M.; Chamkha, A.J.; Raju, S.H. Chemical reaction effects on MHD convective heat and mass transfer flow past a rotating vertical cone embedded in a variable porosity regime. *Afr. Mat.* **2015**, *27*, 645–665. [[CrossRef](#)]

51. Fetecau, C.; Shah, N.A.; Vieru, D. General Solutions for Hydromagnetic Free Convection Flow over an Infinite Plate with Newtonian Heating, Mass Diffusion and Chemical Reaction. *Commun. Theor. Phys.* **2017**, *68*, 768. [[CrossRef](#)]
52. Dawar, A.; Wakif, A.; Thumma, T.; Shah, N.A. Towards a new MHD non-homogeneous convective nanofluid flow model for simulating a rotating inclined thin layer of sodium alginate-based Iron oxide exposed to incident solar energy. *Int. Commun. Heat Mass Transf.* **2021**, *130*, 105800. [[CrossRef](#)]
53. Sabu, A.; Wakif, A.; Areekara, S.; Mathew, A.; Shah, N.A. Significance of nanoparticles' shape and thermo-hydrodynamic slip constraints on MHD alumina-water nanoliquid flows over a rotating heated disk: The passive control approach. *Int. Commun. Heat Mass Transf.* **2021**, *129*, 105711. [[CrossRef](#)]
54. Saba, F.; Ahmed, N.; Khan, U.; Waheed, A.; Rafiq, M.; Mohyud-Din, S.T. Thermophysical Analysis of Water Based (Cu–Al₂O₃) Hybrid Nanofluid in an Asymmetric Channel with Dilating/Squeezing Walls Considering Different Shapes of Nanoparticles. *Appl. Sci.* **2018**, *8*, 1549. [[CrossRef](#)]
55. Sheikholeslami, M.; Ganji, D.D. Nanofluid flow and heat transfer between parallel plates considering Brownian motion using DTM. *Comput. Methods Appl. Mech. Eng.* **2014**, *283*, 651–663. [[CrossRef](#)]
56. Majdalani, J.; Zhou, C.; Dawson, C.A. Two dimensional viscous flows between slowly expanding or contracting walls with weak permeability. *J. Biomech.* **2002**, *35*, 1399–1403. [[CrossRef](#)]
57. Ahmad, S.; Farooq, M.; Mir, N.A.; Anjum, A.; Javed, M. Magneto-hydrodynamic flow of squeezed fluid with binary chemical reaction and activation energy. *J. Cent. South Univ.* **2019**, *26*, 1362–1373. [[CrossRef](#)]